PNAS RESEARCH ARTICLE | APPLIED PHYSICAL SCIENCES

CMOS-compatible reconstructive spectrometers with self-referencing integrated Fabry–Perot resonators

Chunyu You[a,b,c], Xing Li[a,b,c], Yuhang Hu[a,b,c], Ningge Huang[a,b,c], Yang Wang[a,b,c], Binmin Wu[a,b,c], Guobang Jiang[a,b,c], Jiayuan Huang[a,b,c], Ziyu Zhang[a,b,c], Bingxin Chen[d], Yue Wu[a,b,c], Junhan Liu[a,b,c], Xiangzhong Chen[c,e], Enming Song[c,e], Jizhai Cui[a,b,c], Peng Zhou[f], Zengfeng Di[g], Zhenghua An[d], Gaoshan Huang[a,b,c], and Yongfeng Mei[a,b,c,e,1]

Affiliations are included on p. 9.

Edited by John Rogers, Northwestern University–Evanston, Evanston, IL; received February 25, 2024; accepted July 3, 2024

Miniaturized reconstructive spectrometers play a pivotal role in on-chip and portable devices, offering high-resolution spectral measurement through precalibrated spectral responses and AI–driven reconstruction. However, two key challenges persist for practical applications: artificial intervention in algorithm parameters and compatibility with complementary metal-oxide-semiconductor (CMOS) manufacturing. We present a cutting-edge miniaturized reconstructive spectrometer that incorporates a self-adaptive algorithm referenced with Fabry–Perot resonators, delivering precise spectral tests across the visible range. The spectrometers are fabricated with CMOS technology at the wafer scale, achieving a resolution of ~2.5 nm, an average wavelength deviation of ~0.27 nm, and a resolution-to-bandwidth ratio of ~0.46%. Our approach provides a path toward versatile and robust reconstructive miniaturized spectrometers and facilitates their commercialization.

miniaturized spectrometers | Fabry–Perot resonators | silicon nanomembrane | CMOS-compatible integration

Significance

Miniaturized reconstructive spectrometers are poised to revolutionize their application fields through enhanced portability and functionality. However, achieving optimal performance traditionally requires manual tuning of algorithm parameters, and their capability of direct large-scale production using integrated circuit processes remains unproven. In this work, we introduce a miniaturized spectrometer, fully complementary metal-oxide-semiconductor-compatible and enhanced with self-referencing Fabry–Perot resonators, eliminating manual tuning of algorithms for optimal performance. This work demonstrates wafer-scale production of universal and robust miniaturized spectrometers with a self-adaptive reconstructive algorithm, signifying its potential for commercialization and extensive interdisciplinary application.

Optical spectrometers are an indispensable analytical tool used extensively in scientific and industrial research for characterization across diverse fields (1–3). Of particular interest is the miniaturization of spectrometers (4–7) for great potential in diverse disciplines in, e.g., machine vision (8, 9), environmental monitoring (10, 11), and medical diagnostics (7, 12). Recent developments have showcased the emergence of miniaturized spectrometers featuring innovative material systems and device designs (13). Notable examples include nanowires with variable bandgaps (14), black phosphorus nanosheets with tunable Stark effects (15), tunable van der Waals junctions (16, 17), and photonic crystal arrays (18, 19), all of which exhibit performance levels comparable to their bulkier commercial counterparts in certain scenarios.

A critical driver of these advancements lies in the deployment of reconstruction algorithms, harnessing the progress in mathematics (20, 21), and compressive sensing techniques (13, 14) These algorithms help overcome the tradeoff between sample number and performance caused by miniaturization (13), also known as the Nyquist–Shannon limitation (14). Methods such as least absolute shrinkage and selection operator (LASSO) (15, 22), Tikhonov regularization (14, 16), and total-variation regularization (23, 24) have been applied to achieve high-performance reconstruction. Nonetheless, the quality of reconstructed spectra is heavily reliant on the precise selection of algorithm parameters (16, 25, 26), such as kernel functions and learning rates. Suboptimal parameter choices can distort reconstructed spectra, limiting their versatility across spectrum types and diminishing their usability in real-world applications (27).

On the other hand, mass production also presents a barrier to commercializing miniaturized reconstructive spectrometers (13, 28). The novel materials being explored could not be easily integrated with high-volume complementary metal-oxide-semiconductor (CMOS) fabrication processes commonly used in the semiconductor industry (5, 29–31). As a result, translating these lab-scale spectrometers into manufacturable devices with robustness, repeatability, and economies of scale remains a challenge since standard semiconductor manufacturing processes cannot be fully leveraged in fabricating the miniaturized spectrometers (32, 33).

Here, we present a miniaturized spectrometer design that integrates the merits of both conventional and reconstructive spectrometers. This enables bilevel optimization in reconstructing spectra, creating a self-adaptive algorithm that provides accurate results universally across diverse spectral types. Specifically, we choose Fabry–Perot (FP) cavities integrated with silicon-nanomembrane (Si-NM) photodetector arrays to form a miniaturized spectrometer as an example due to the excellent CMOS-compatible process. This work demonstrates the

Author contributions: C.Y., J.C., G.H., and Y.M. designed research; C.Y., X.L., Y.H., N.H., B.W., and B.C. performed research; P.Z., Z.D., Z.A., and Y.M. contributed new reagents/analytic tools; C.Y., Y.H., Y. Wang, B.W., G.J., J.H., Z.Z., Y. Wu, J.L., X.C., E.S., J.C., and Y.M. analyzed data; and C.Y., G.H., and Y.M. wrote the paper.

The authors declare no competing interest.

This article is a PNAS Direct Submission.

[1]To whom correspondence may be addressed. Email: yfm@fudan.edu.cn.

This article contains supporting information online at https://www.pnas.org/lookup/suppl/doi:10.1073/pnas.2403950121/-/DCSupplemental.

Published August 8, 2024.

wafer-scale production of universal and robust miniaturized spectrometers with a self-adaptive reconstructive algorithm. By using a single unified algorithm without human parameter adjustment, this miniaturized spectrometer performs accurate reconstruction of both monochromatic and complex broadband spectra, as well as hyperspectral imaging.

Results

Working Principle and Device Design. Fig. 1*A* illustrates the working principle of a conventional spectrometer utilizing narrow bandpass filters to discriminate different wavelengths. The intensity at each wavelength is directly measured based on the amount of light that passes through the corresponding filter. This process can be described as "point to point", resulting in a coarse but relatively accurate spectrum. Fig. 1*B* depicts the working principle of a typical reconstructive spectrometer. The spectrometer encodes the unknown spectrum into collected data. These data are then reconstructed into a spectrum through a supervised algorithm with parameters Φ. The algorithm finds the minimum cost function in the spectrum parameter space S, often via regularization methods like Tikhonov or total variation (14, 16, 23, 24). While this reconstruction can achieve high-resolution spectra, the result may be unstable since different choice Φ can lead to different minimum cost functions (24). It should be noted that while some regularization methods use constraints like generalized cross-validation (GCV) to optimize parameters (14, 26), key algorithm parameters like kernel functions and learning rate still rely heavily on human input (15, 16).

Fig. 1*C* demonstrates the working principle of a present self-adaptive spectrometer. In addition to encoding the spectrum into data for the algorithm, a coarse self-reference spectrum is provided by the spectrometer in a conventional manner. With this self-reference, a bilevel optimization can be achieved across both the spectrum parameter space S and algorithm parameter space Φ, and thus, the search for the minimum cost function encompasses higher dimensions. This enables identification of the global minimum cost function to reconstruct an accurate and stable spectrum through the automatic selection of the most optimal parameters.

The whole device is CMOS-compatible and can be fabricated through a wafer-scale process Fig. 1*D* shows the photodetector arrays fabricated on a 2-inch wafer before the FP cavity growth. Owing to the mature CMOS process, the resulting miniaturized spectrometer has a satisfying small footprint. Fig. 1*E* demonstrates a photograph of such a device on a fingertip. It is worth mentioning that the current size is limited by the feature size of the laboratory mask aligner, and by utilizing an industry-standard chip process with much smaller feature sizes, we can further shrink the size of the device. Fig. 1*F* shows the reconstruction results by using this self-adaptive spectrometer for some quasi-monochromatic lights, with a line width of approximately 6 nm, which match quite well with the results obtained from a commercial spectrometer. Although

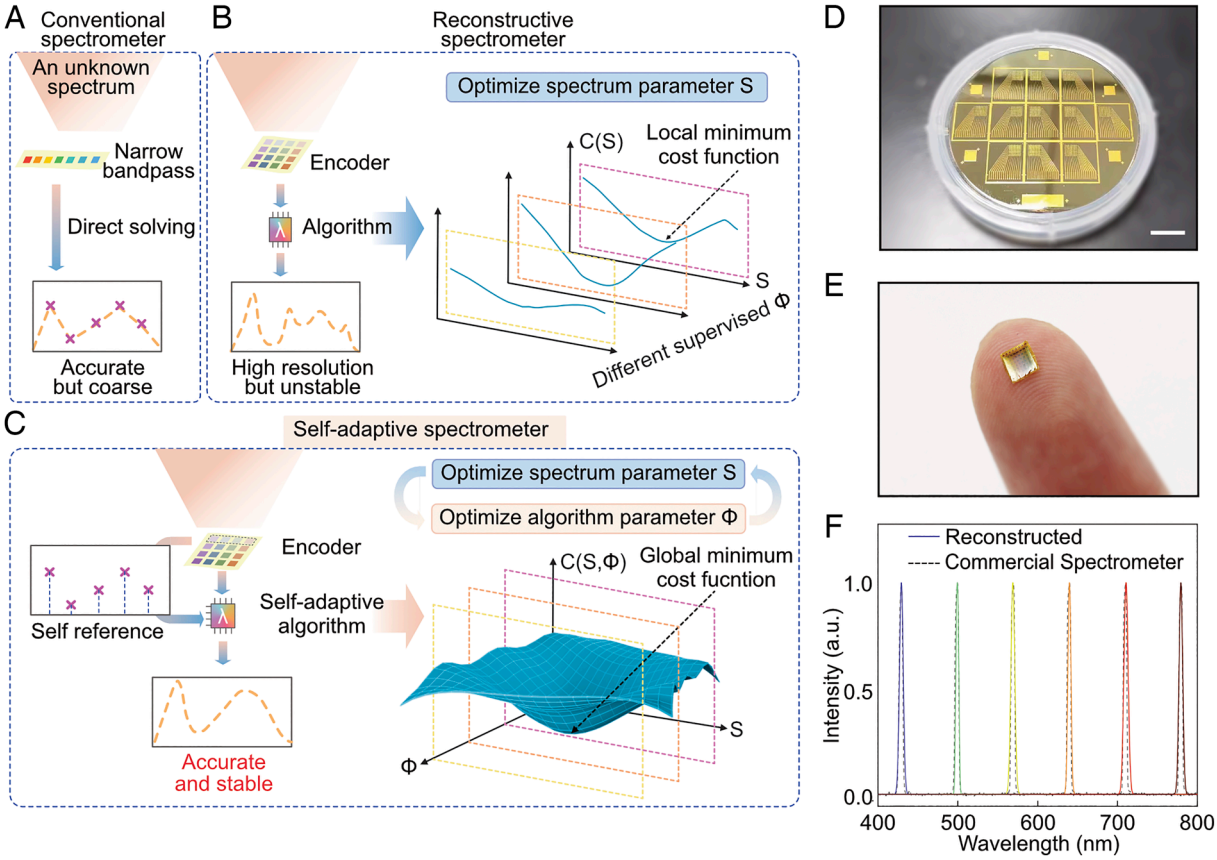

Fig. 1. Self-adaptive spectrometer miniaturized by the wafer-scale process. (*A*) Working principle of a conventional spectrometer with narrow bandpass filters to discriminate different wavelengths. (*B*) Working principle of a typical reconstructive spectrometer: The unknown spectrum is encoded into data which an algorithm reconstructs into a spectrum. The algorithm finds a minimum cost function in spectrum parameter space S under supervised algorithm parameter Φ. The result depends on the chosen Φ. (*C*) Working principle of a self-adaptive spectrometer: In addition to encoding the spectrum and passing the data to the algorithm, the spectrometer also provides a coarse self-reference spectrum collected by using conventional methods. This self-reference guides the algorithm parameters to yield an accurate and stable result. The algorithm identifies the global minimum cost function across parameter spaces S and Φ. (*D*) The wafer-scale fabrication of the miniaturized spectrometer. (The scale bar is 1 cm.) (*E*) The result miniaturized spectrometer on a fingertip. (*F*) Pseudo-monochromatic spectra reconstructed from our spectrometer from our self-adaptive miniaturized spectrometer utilizing all encoder channels (solid curves) and measured by a commercial spectrometer (dash curves). The line width of the input quasi-monochromatic light is approximately 6 nm.

the miniaturized spectrometer we obtained has a very small size, it still has excellent performance. Specific spectral resolution metrics are discussed in more detail later.

CMOS-Compatible Integration of FP Cavities. Fig. 2*A* outlines the manufacturing process for the self-adaptive spectrometer, entailing the following steps: 1) The process begins with an n-type Silicon-On-Insulator (SOI) wafer. 2) The p-doped region is created through photolithography followed by ion implantation or thermal diffusion, establishing P-N junctions. 3) Further photolithography and reactive ion etching (RIE) techniques define the active region and segregate each photodetector. 4) SiO_2 deposition via plasma enhanced chemical vapor deposition (PECVD) is employed to passivate the surface. 5) Via 1 for metal contact is formed using photolithography and HF etching. 6) The first metal layer is applied through photolithography and sputtering. 7) A photosensitive polyimide (PI) interlayer is then spin-coated, serving as a low dielectric constant insulator for electrodes. 8) Via 2 is outlined via photolithography. 9) The second metal layer is added using photolithography and sputtering. 10) The wafer is adhered to a Kapton film with Kwik-Sil and PI. 11) Subsequently, the wafer is flipped, and the handle silicon is removed through inductively coupled plasma reactive ion etching (ICP-RIE) and XeF_2 etching, with photolithography and RIE creating via 3 for signal readout. 12) Finally, multiple FP cavities are directly fabricated onto the buried oxide layer of the wafer

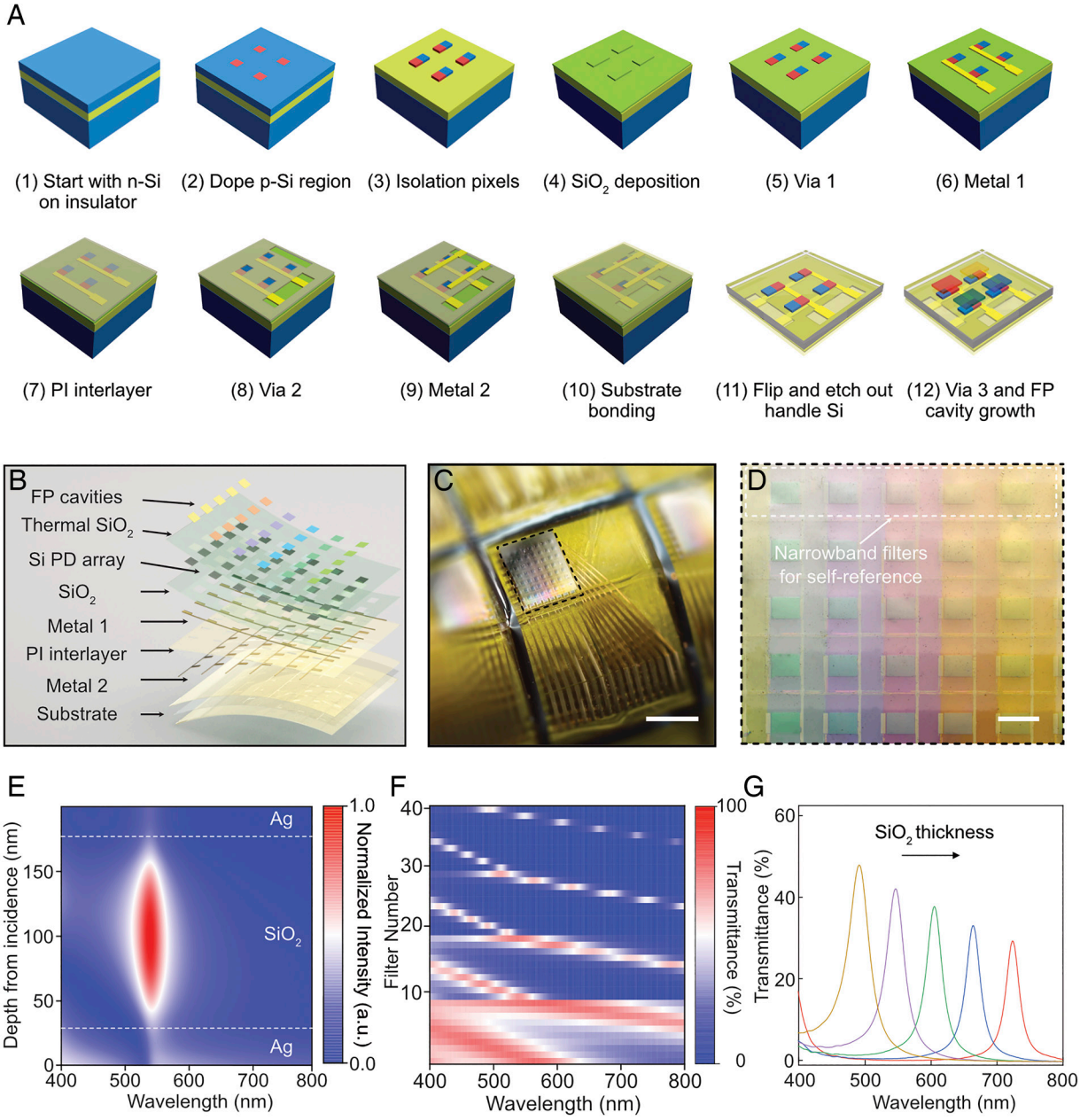

Fig. 2. CMOS-compatible fabrication of self-adaptive spectrometers, featuring seamless integration of optical cavities with tailored transmittance control (*A*) Procedures of the fabrication process of Si-NM photodetector array. (*B*) Schematic illustration of key functional layers of the self-adaptive miniaturized spectrometer within an exploded view. (*C*) Photo of a single miniaturized spectrometer with fan-out electrodes. (The scale bar is 2 mm.) (*D*) Optical image of the integrated FP cavities on photodetector array showing designed color gradient in horizontal direction and color purity gradient in vertical direction. Cavities with the highest color purity (greatest metal thickness) are designated for narrowband self-reference input. (The scale bar is 200 μm.) (*E*) A finite element analysis of optical field distributions in a typical cavity, highlighting strong resonance at 520 nm with a SiO_2 thickness of 150 nm. (*F*) Color contour plot of the transmittance of FP cavities of a 4 × 10 array with designed transmittance. (*G*) Typical transmittance characteristics of FP cavities with Ag thickness of 40 nm and SiO_2 thickness of 130 to 210 nm with a step of 20 nm.

in a single batch process. This comprehensive process, fully compatible with established semiconductor industry equipment and adhering to CMOS standards, renders the spectrometer ready for commercial production.

The completed self-adaptive spectrometer comprises the components illustrated in Fig. 2*B*: 1) A top layer featuring arrays of diverse FP cavities. 2) A thermal SiO_2 layer, derived from the buried oxide layer of the SOI wafer, electrically and optically isolates the FP cavities from the photodetector layers. 3) Si-NM photodetector arrays, coupled with SiO_2 for surface encapsulation. 4) Two metal wire layers function as the bit and word wires for spectrum detection channel multiplexing, while a PI interlayer acts as a low dielectric constant insulator. 5) A substrate composed of ultrathin PI, Kwik-Sil, and Kapton film is designed for exceptional flexibility and to mitigate strain across the inorganic layers mentioned above. A detailed schematic cross-section of this miniaturized spectrometer is provided in *SI Appendix*, Fig. S1. The mechanically flexible design of the spectrometer may be particularly advantageous for biomedical engineering applications, such as individual cell analysis and implantable cancer detection.

An optical image of the completed device is presented in Fig. 2*C*. The rainbow color pattern observed at the center of the device is attributed to the FP cavities. Fig. 2*D* shows the amplified view of the FP cavities integrated on the photodetector arrays. The image shows two types of optical property variations of the FP cavity array. Horizontally, optical cavities have an obvious change in the transmission (and reflection) peak wavelengths, thus exhibiting different colors. Vertically along the image, the color purity or monochromaticity changes gradually, which is caused by the change in the transmission peak width of the microcavity. Experimentally, the position of the transmission peak wavelength can be tuned by controlling the thickness of the dielectric layer (SiO_2) constituting the FP cavity, while the monochromaticity can be tuned by controlling the thickness of the top and bottom metal reflective layers sandwiching the dielectric layer. Cavities with the highest color purity (greatest metal thickness) are designated for narrowband self-reference input. FP cavities featuring a metal-oxide-metal structure are employed here due to their straightforward fabrication process and the wide bandwidth they offer.

A finite element analysis of the sandwiched structure gives an intuitionistic understanding of the mechanics of the cavities' wavelength discrimination behavior (Fig. 2*E*). An FP mode resonance occurs when the phase change of the light wave after a round trip inside the SiO_2 layer cavity is 2π with the first resonant mode, while the higher resonance modes with an integer multiple of 2π. Owing to the low absorption of silver in the visible light region, a transmittance peak occurs. Fig. 2*F* demonstrates the collective transmittance spectrum of 40 selected FP cavities (a 4 × 10 array) which are identical to those integrated on the final device (detailed transmittance data of each channel are shown in *SI Appendix*, Fig. S4). The upper region of the image represents those with a thicker silver thickness while the lower region represents the thinner ones. The thickness of the silver varies by groups: starting at 10 nm for filters #1 to 10, increasing to 20 nm for filters #11 to 20, 30 nm for filters #21 to 30, and peaking at 40 nm for filters #31-40. Following this, the SiO_2 layers start with a thickness of 270 nm for filters #1, #11, #21, and #31, and the thickness decreases progressively by 20 nm for each subsequent group, culminating in a final thickness of 90 nm for filters #10, #20, #30, and #40. Fig. 2*G* shows detailed transmittance spectra of 5 typical FP cavities with a 40 nm silver layer. The increased transmittance of all these cavities in the near ultraviolet region occurs due to silver's inherently higher transmittance at shorter wavelengths.

Self-Adaptive Spectrum Reconstruction. Fig. 3*A* depicts the self-adaptive spectrum reconstruction process achieved by our miniaturized spectrometer. Our miniaturized spectrometer has an additional set of narrowband channels for conventional spectrum measurement; thus, it provides two datasets of current for sensing the spectrum (*SI Appendix*). The first set is the currents from the narrowband response channels, which can be considered as the scalar product of the spectral intensity at a certain band and the response of the channel responsible for that band, from which a definite but coarse spectrum can be easily obtained. The second set is the currents from all channels (including the narrowband ones), which is the integral result of multiplying the spectrum at each wavelength by the channel's response:

$$\int_{\lambda_{\min}}^{\lambda_{\max}} S(\lambda) \cdot R_i(\lambda) d\lambda = I_i, \quad [1]$$

where, $\lambda_{\min}$ and $\lambda_{\max}$ define the spectrometer's operational wavelength range, $S(\lambda)$ is the unknown spectrum, $R_i(\lambda)$ is the responsivity of each channel, and I_i is the current output of each channel. This can also be seen as the inner product of two high-dimensional vectors computationally:

$$R_{m\times n} \times S_{n\times 1} = I_{m\times 1}, \quad [2]$$

where m represents the number of channels, and n represents the quantity of spectral segmentation (higher n means higher resolution). According to compressive sensing theory, the minimum required number of channels m can be estimated from

$$\mathrm{m} \approx C \cdot K \log(\mathrm{n}/K), \quad [3]$$

where a signal's sparsity in the transform domain is K, and C is a constant related to the signal and the reconstruction algorithm, typically taken as 1. If we aim to reconstruct the visible light spectrum (400 to 800 nm) with an accuracy of about 1 nm, we can assume n is 400. Considering that the spectrum can be reasonably approximated by the superposition of 10 Gaussian functions, we can calculate that $m \approx 36$. We incorporated a slight redundancy, which is why we initially opted for 40 channels in our reconstruction.

Through traditional iterative methods, it is impossible to reconstruct the spectrum from the currents, owing to the high dimensionality of the vectors themselves and the inevitable noise in practical tests that makes the equations ill-posed (20, 21). By adopting Tikhonov regularization and other methods (13, 34), more credible solutions can be obtained, but they vary greatly with different algorithm parameters. In fact, different spectral shapes need different parameters to get optimal solutions, which have been well discussed in other literatures (16, 25, 26). Here, we introduce the spectral result obtained from the first dataset as a self-reference for the computational solution from the second current set, through which the algorithm adjusts various parameters by itself and obtains a stable result close to the real spectrum via inherent iterations. *SI Appendix,* Fig. S11 for more details on the algorithm workflow. Fig. 3*B* shows the overall responsivity across all channels utilized in our miniaturized spectrometer within the visible light range and Fig. 3*C* shows responses of typical channels, specifically channels #2, #12, #22, and #32. The final responsivity can be considered the element-wise product of the intrinsic responsivity of the Si-NM photodetectors and the transmittance of the FP cavities. Detailed response of each channel is demonstrated in *SI Appendix*, Fig. S12. Using the precalibrated

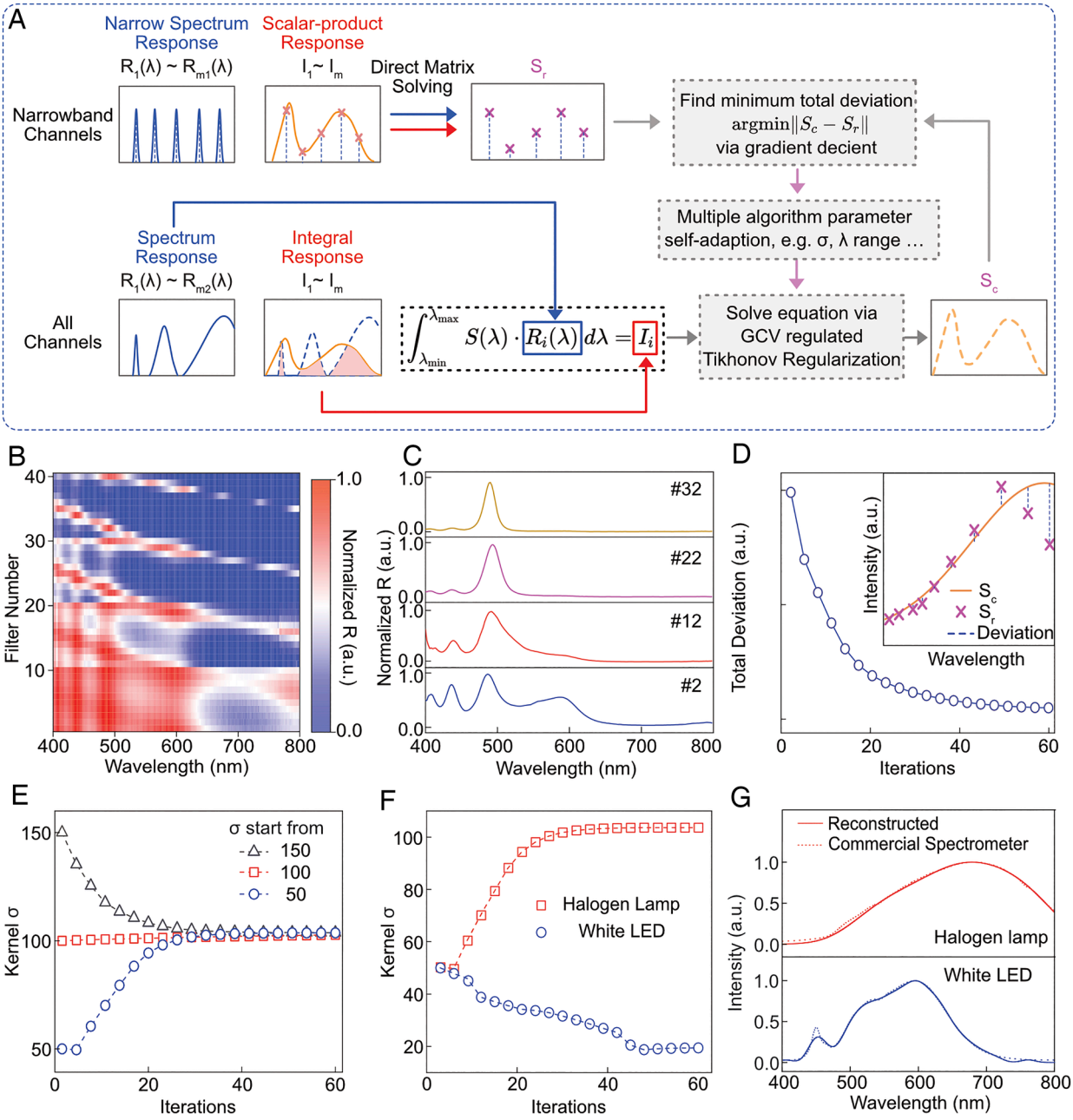

Fig. 3. Self-adaptive spectrum reconstruction utilizing both conventional and computational methods. (*A*) Schematic illustration of the self-adaptive algorithm. (*B*) Color contour plot of the spectral response matrix of the device. (*C*) Spectral response of typical channels presented in (*B*). (*D*) Total Deviation between the halogen lamp's reconstructed spectrum (kernel σ = 150) and the spectrum calculated from narrowband channels across self-adaptation iterations. The inset shows the reconstructed spectrum, the directly calculated spectrum from the narrowband channels, and their corresponding deviations. (*E*) Convergence of Kernel σ to ~100 across self-adaptation iterations with varying initial values in the reconstruction of a halogen lamp spectrum. (*F*) Kernel σ convergence to distinct values in the reconstruction of halogen lamp and white LED spectra, starting from the same initial value. (*G*) Reconstructed spectra (solid curves) at various selected iterations and the final outcomes for a halogen lamp and a white LED. Dashed curves show the results measured by a commercial spectrometer.

spectrum responses of the channels and the workflow in Fig. 3*A*, we can reconstruct unknown spectrum in the visible light region, as long as these spectra can be transformed into sparse vectors.

Fig. 3*D* serves as an example of reconstructing a halogen lamp spectrum, depicting the deviation between the reconstructed spectrum (with a kernel function parameter, σ, of 150) and the spectrum directly calculated from narrowband channels. The inset clarifies this comparison, spotlighting both the reconstructed and directly calculated spectra, along with the method for determining their respective deviations. A standard gradient descent process is utilized to minimize this total deviation, thereby optimizing the Kernel σ. Fig. 3*E* demonstrates that Kernel σ, irrespective of its initial values, tends to stabilize around 100 in the reconstruction process for a halogen lamp spectrum. Moreover, Fig. 3*F* illustrates the convergence of Kernel σ to distinct values in the spectral reconstruction of both halogen lamp and white LED, starting from the same initial value. The corresponding reconstructed spectra are presented in Fig. 3*G*. We have also tested the system with common light sources such as Xenon, incandescent, fluorescent, and mercury lamps (*SI Appendix*, Fig. S17). These outcomes emphasize the robustness and versatility of our approach. Unlike monochromatic sources, these broadband lights are typically challenging targets for miniaturized spectrometers to reconstruct due to their complex spectral details (14, 25). Our spectrometer autonomously selects optimal algorithm parameters through a bilevel optimization process that considers both spectrum and algorithm

parameters, achieving superior performance compared to reconstructions using arbitrary parameter selections, all without the need for external supervision or manual adjustment (*SI Appendix*).

By combining narrowband and broadband channels, our miniaturized spectrometer has demonstrated exceptional spectral reconstruction capabilities, significantly surpassing the performance achieved by using only narrowband channels (*SI Appendix*, Fig. S18). The impact of the number of self-referencing channels on adaptive reconstruction, especially regarding its convergence, is illustrated in *SI Appendix*, Fig. S19. We adopted 10 self-reference channels with the FWHM (full width of half maximum) of around 36 nm to cover the whole calculating spectrum from 400 nm to 800 nm. More reference channels like 15 could lead to an unnecessary overlap between referenced wavelength positions and might induce errors in calculation. It is noteworthy that although the structure of the FP cavity is sensitive to the angle of incidence, our miniaturized spectrometer can still accurately reconstruct the spectrum when the angle of incidence is known (*SI Appendix*, Figs. S20–S22). Additionally, when the incident light is known, such as in cases of monochromatic light, we can leverage their angle dependence to reconstruct the direction of the incoming light (*SI Appendix*, Figs. S23 and S24).

Performance of the Self-Adaptive Miniaturized Spectrometer. Wavelength resolution is a key parameter for spectrometers, especially for applications like wavelength meters or high-precision material identification. It is entirely feasible to record a high-precision response matrix in advance to provide more precise spectrum reconstruction since the response matrix can be collected prior to spectrum testing. However, a larger response matrix introduces a great challenge of a significantly increased computational load on the backend. If a channel does not sufficiently respond to the spectrum under test, removing it will not impact the system's performance and will simplify subsequent reconstruction calculations. For example, if we measure the spectral range between 400 nm and 500 nm, only effective channels among it are counted to reduce the computational load with the same level of accuracy. By automatically masking nonresponsive bands, our miniaturized spectrometer can invoke a high-density response matrix within the band of interest to complete subsequent calculations. During this process, the dimensions of the response matrix used for reconstruction are adjusted automatically without manual intervention. (*SI Appendix*, Fig. S25).

Fig. 4*A* shows an example of a high-density spectral response matrix in a 10 nm band of interest from 488 to 498 nm. The matrix has a finely calibrated step size of just 0.1 nm per step. The detailed responses of typical channels, namely channels #2, #12, #22, and #32, are featured in Fig. 4*B* Using this high-resolution response matrix, we accurately reconstructed monochromatic light sources (Fig. 4*C*). If a coarser response matrix is used, such as one calibrated at 5 nm intervals, the reconstruction results for monochromatic light and other fine spectra will significantly deteriorate. This outcome is demonstrated in *SI Appendix*, Fig. S27. Fig. 4*D* shows the comparison between input peak wavelengths and output reconstructed peak wavelengths, exhibiting a good agreement. We further analyzed the deviation of our miniaturized spectrometer (Fig. 4*E*) and calculated the resolution at a given input peak wavelength λ: $R_\lambda = \lambda/\Delta\lambda$. Thus, we achieved an average wavelength deviation of approximately 0.27 nm and a resolving power as high as 5,806.

We further apply the traditional spectrometer resolution test on our miniaturized spectrometer: illuminating two monochromatic peaks simultaneously onto our spectrometer and gradually reducing the spacing between them to study the minimum spacing

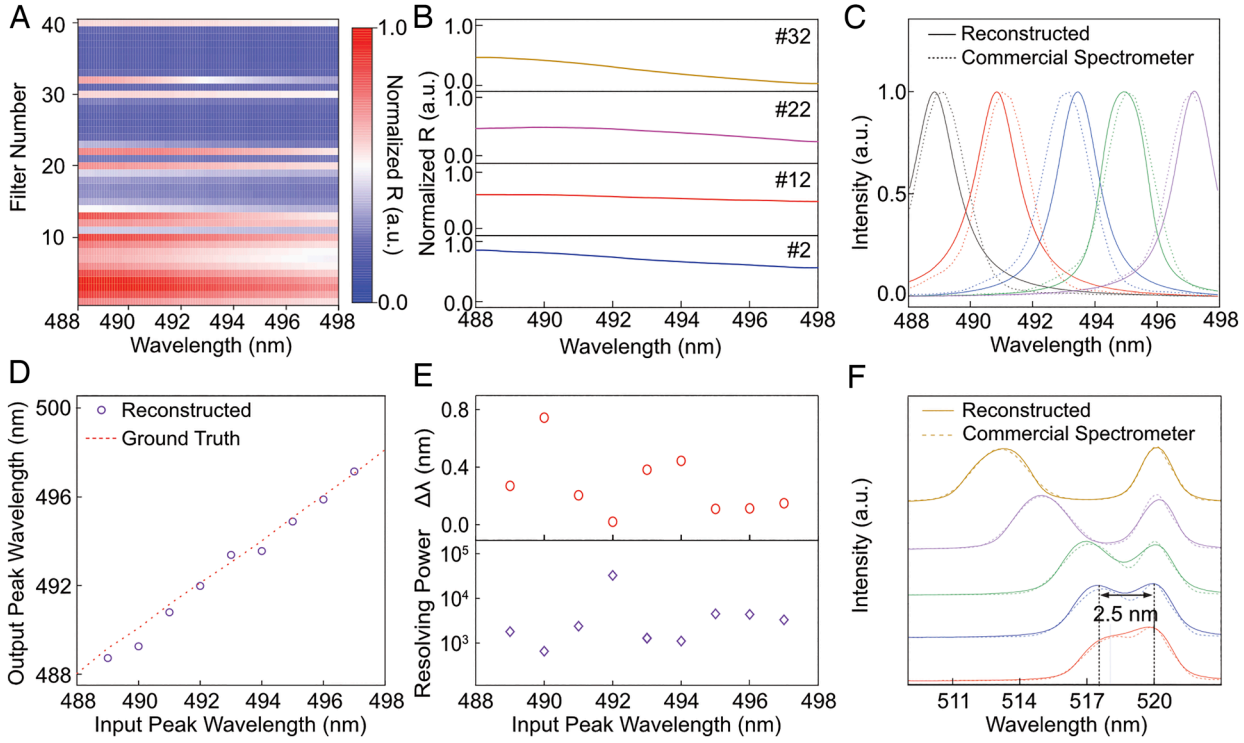

Fig. 4. High performance of the miniaturized spectrometer. (*A*) Color contour plot of the high-density spectral response matrix after automatically masking nonresponsive bands. (*B*) Spectral response of typical channels presented in (*A*). (*C*) Monochromatic spectra reconstructed with our spectrometer (solid curves) and measured by using a commercial spectrometer (dashed curves). (*D*) Peak wavelengths of the reconstructed spectra versus ground truth input peak wavelength. (*E*) Deviation of reconstructed peak wavelengths (*Top*) and calculated wavelength resolving power. (*F*) Spectra of the mixture of two monochromatic light sources reconstructed with our spectrometer (solid curves) and measured by using a commercial spectrometer (dashed curves). The dotted vertical lines mark the locations of the resolvable dual incident peaks, which are separated with a wavelength distance of 2.5 nm.

at which our spectrometer can still resolve the two spectral lines (The experimental setup is shown in *SI Appendix*, Fig. S26). As shown in Fig. 4*F*, two peaks near ~518 nm with a separation of 2.5 nm can be distinguished. This result indicates that our miniaturized spectrometer has performance comparable to that of commercial fiber optic spectrometers and other miniaturized spectrometers, while having orders of magnitude improvements in size and cost (*SI Appendix*).

Applications of Miniaturized Spectroscopy. The ultrasmall footprint of our miniaturized spectrometer enables potential uses. Traditionally, transmittance, absorption, and PL spectroscopy have been most widely used for their ability to determine matter and study electron structure (3), and here they can be performed in a miniaturized fashion. Fig. 5*A* depicts a scenario for transmission and absorption spectroscopies with a highly miniaturized setup by combining a microfluidic device and a broadband mini-LED. Here, we use two miniaturized spectrometers—one behind the sample droplet and the other behind the blank channel as a reference. This allows us to obtain two sets of current data, which were used to generate two spectra, i.e., S_{sample} and S_{ref}. Thus, the transmittance of the sample is easily calculated as $T = S_{sample}/S_{ref}$. Similar to conventional ultraviolet (UV)-visible spectrophotometry (3), reflection from the sample is not considered in this testing configuration, thus the absorbance can be expressed through Beer–Lambert law as $A = \log(1/T)$. Here, Fig. 5*B* shows the transmittance spectra of vitamin B12 (cyanocobalamin) at a concentration of 0 to 0.6 mg/L, and Fig. 5*C* depicts the corresponding absorbance spectrum. The reconstruction results match well with those from a commercial spectrometer, demonstrating a good reliability of our setup. In the scenario of the PL test (Fig. 5*D*), a UV mini-LED is used to excite PL from the sample in the microfluidic channel. A bandpass filter is placed in front of the miniaturized spectrometer so that the excitation light is blocked while the excited PL light can transmit through and illuminate the spectrometer. Fig. 5 *E* and *F* show the reconstruction results from our miniaturized spectrometer for two common photoluminescence probes in

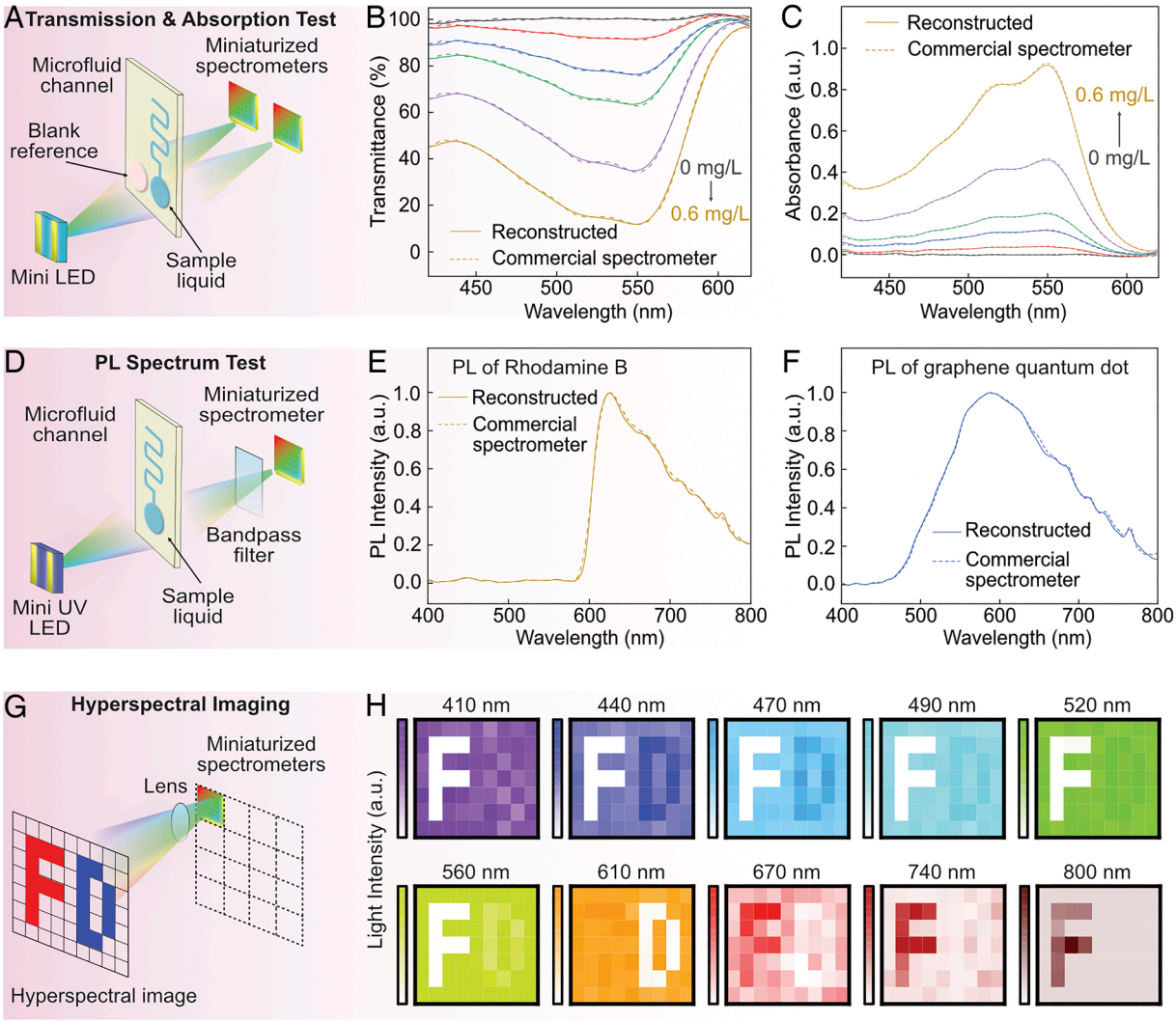

Fig. 5. Applications of miniaturized spectroscopy. (*A*) Configuration of miniaturized transmission and absorption tests by using a microfluidic channel as a liquid cuvette. A broadband mini-LED serves as the light source and two miniaturized spectrometers are utilized: one to collect the sample signal and the other for blank control. (*B*) Transmittance spectra obtained from our spectrometer (solid curves) and a commercial spectrometer (dash curves) of vitamin B12 solutions of different concentrations. (*C*) Absorption spectra calculated from (*B*). (*D*) Configuration of the miniaturized PL test. A microfluidic channel functions as the liquid cuvette, a mini UV-LED provides excitation, and a bandpass filter transmits PL while rejecting excitation light. (*E*) PL spectra obtained from our spectrometer (solid curve) and a commercial spectrometer (dash curve) for a rhodamine B solution of 5 mg/L. (*F*) PL spectra obtained from our spectrometer (solid curve) and a commercial spectrometer (dash curve) for a graphene quantum dot solution of 1 mg/mL. (*G*) Configuration of the hyperspectral imaging of our miniaturized spectrometer using single-pixel scanning. A broadband light source modified with red and blue color filters is focused through a lens and incident to the spectrometer pixel. (*H*) Hyperspectral images reconstructed at different wavelengths. The pixel intensity is normalized within each pixel.

the lab, i.e., rhodamine B and graphene quantum dots. One can also notice the good consistency with the results obtained from a commercial spectrometer.

A widely anticipated application of miniaturized spectrometers is engagement in hyperspectral cameras as individual pixels, enabling acquisition of spectral information across the entire image with a single shot. Our miniaturized spectrometer is highly compatible with advanced CMOS processes and can be mass-produced at the wafer scale, making it particularly suitable for such applications. Here, we demonstrate proof-of-concept hyperspectral imaging through single-pixel scanning (Fig. 5*G*). The imaging target here is a pattern with the letters "FD", where the "F" and "D" regions are modified with different optical filters, while the rest of the image is almost completely transparent to visible light. With a white-light LED as backlight, a series of photocurrent data scanned at different positions with different channels are collected (*SI Appendix*, Fig. S28), forming a photocurrent data cube, and through the self-adaptive reconstruction process, a spectral-space data cube is achieved. Each pixel in the obtained hyperspectral image has a full spectrum associated with it. Fig. 5*H* shows the normalized spectral intensity at different wavelengths across the image. The spectral images show that the red filter blocks nearly all wavelengths from 410 nm to 560 nm. In contrast, the blue filter primarily absorbs light from 610 nm to 670 nm, while still transmits near-infrared light at 800 nm. This information cannot be obtained by conventional RGB or RYYB cameras or the human eyes. Similar absorption profiling capability has widespread applications in areas like rapid material detection and pharmaceutical analysis, expanding the immense potential of hyperspectral imaging.

Discussion

We introduce a unique approach that combines the advantages of conventional and computational spectrometers to achieve robust and accurate spectral reconstruction automatically, without the human supervision required in previous works. The entire system can be manufactured at the wafer scale by using the mature CMOS process, which is encouraging for reducing the traditionally high costs of spectrometer devices. An estimation of the cost for mass production of the self-adaptive miniaturized spectrometer chips is detailed in *SI Appendix*. Meanwhile, the mass production capability enables exploring their applications in areas such as medical testing, agricultural inspection, and smart dust (35). Furthermore, the size of the spectrometer could be significantly reduced by employing a mature 130-nm technology node (36). It allows the cavity pixel pitch to be compacted to a small size of around 3 μm, which is the limit for effective resonance characters of FP cavities without introducing lateral effects (*SI Appendix*, Fig. S29). A 0.5 μm spacing could be sufficient for both pixel separation (*SI Appendix*, Fig. S30) and accommodating the readout circuit (37), allowing a single channel to fit within a 3.5 × 3.5 μm^2 area. As a result, a spectrometer designed with 64 channels (8 × 8) could be compacted to an impressively small size down to around 28 × 28 μm^2. It should be noted that as the volume decreases, the device's signal-to-noise ratio, dynamic range, and response speed will experience degradation. Therefore, a balance between footprint and performance should be determined based on actual requirements.

We demonstrate results using a platform of Si-NM phototransistors and FP cavities, owing to their reliable performance and wafer-scale fabrication capabilities (38–40). FP cavities can be regarded as easily fabricated optical microcavities that readily attain the effect of narrowband filters used in conventional spectrometers. Moreover, it should be noted that with interdisciplinary advances, both the photodetection layer and the spectrum regulating layer could be replaced. For instance, 2D materials with excellent optoelectrical properties (29, 41), like MoS_2 and WSe_2, could substitute for Si-NM. Likewise, novel photonic structures, including Bragg reflectors (42, 43) and photonic crystals (37), could replace the FP cavities. Thus, our approach is versatile and readily adaptable.

A trend in miniaturized spectrometers is adopting tunable or reconfigurable components (13, 44), such as tunable filters (45) or detectors (17). Specifically, our reconfigurability lies in the algorithm, which is often fixed in previous works (16, 25, 26). The bilevel self-adaptive algorithm, enabled by the fusion of conventional and computational schemes, demonstrates great flexibility in reconstructing diverse spectral types. Moreover, while lack of hardware reconfigurability does hinder footprint reduction, emerging technologies like single-pixel imaging could mitigate this (46, 47). Moreover, in modern optoelectronics, the signal processing units rather than the sensors tend to dominate size (36, 48).

In conclusion, our miniaturized spectrometer system delivers great spectrum reconstruction ability while maintaining the compatibility of wafer-scale fabrication. This work offers a possible approach for computational spectrometer design to improve their robustness and versatility toward different types of spectra.

Materials and Methods

Fabrication of the Device. Fabrication began with a weakly p-doped SOI wafer (Soitec) comprising a 1,000 nm top silicon layer, 2,000 nm buried oxide layer, and 725 μm handle substrate. High-temperature (1,100 °C) diffusion doping formed the ~10^{19} cm^{-3} doped region. Photolithography and RIE defined the Si-NM patterns for each phototransistor functional region. Plasma-enhanced chemical vapor deposition (PECVD) and atomic layer deposition (ALD) deposited a SiO_2/Al_2O_3 stack gate dielectric (50/15 nm thickness). After opening vias through the dielectric at the source/drain regions, sputtering yielded 5/150 nm Cr/Au (first layer) and 10/500 nm Cr/Au (second layer). Photolithography and wet etching patterned the metal to form gate electrodes and interconnects. Spin coating of 1.6 μm photosensitive polyimide, patterned by photolithography, created a low dielectric constant insulator separating metal layers. Spin coating of ~2 μm polyimide was used as a buffer layer at the interface, and the device was then bonded to a ~14 μm Kapton film (DuPont) by using Kwik-Sil (World Precision Instruments). The handle layer was then removed by SF_6/O_2 inductively coupled plasma (ICP) RIE and XeF_2 etching after flipping the samples. Finally, photolithography and RIE opened contact windows in the BOX layer, completing the fabrication process. FP cavities were then grown with a lab-modified e-beam evaporator with two linear stepper motors. One motor was used for deposition of stepped Ag reflective layers with thicknesses of 10 to 40 nm (step: 10 nm), while the other was used for deposition of stepped SiO_2 layer with thicknesses of 90 to 270 nm (step: 20 nm). Two hardmasks were used to define the FP cavity regions.

Optoelectronic Performance Tests. Output and transfer properties were characterized by using a precise source meter (Keysight B2902B). Optoelectronic performance was evaluated under 450 nm laser irradiation (Lei Ze Electronics) modulated via optical attenuators (Oeabt Optics). Irradiation power was calibrated with an optical power meter (Thorlabs PM100D). Responsivity time was measured on an oscilloscope (Tektronix TBS2000) with a pulsed laser irradiation modulated by a signal generator (Keysight 33500B). The response matrix was calibrated by using a tunable light source with an exit slit of 1 mm or 0.1 mm (Zolix TLS300X). Electrical signals were amplified (SRS 570) and measured on a lock-in amplifier (SRS 830) while modulated with an optical chopper (SRS 540). The response matrix calibration was automated through a LabVIEW program. Noise spectral density was tested by using a semiconductor parameter analyzer (Primarius FS-Pro).

Reconstruction of Spectra. Quasi-monochromatic light was provided by a tunable light source (Zolix TLS300X) with a 2 mm exit slit. Complex broadband spectra were provided by a halogen lamp and a white LED (both from Ideaoptics). The dual-peak spectrum for spectral resolution testing was generated by combining tunable light around 520 nm with a 520 nm laser. Their intensities were modulated via attenuators. Reference spectra were measured by using a fiber spectrometer (Ideaoptics PG2000-Pro) for comparison with reconstruction results. Current data from the miniaturized spectrometer were processed through a MATLAB program to achieve the reconstructed spectra.

Data, Materials, and Software Availability. All study data are included in the article and/or *SI Appendix*.

ACKNOWLEDGMENTS. Part of the sample fabrication was performed at the Fudan Nano-fabrication Laboratory and Soft Matter Nanofab of Shanghai Tech University. This work is supported by the National Key Technologies R&D Program of China (2021YFE0191800 to Y.M. and 2021YFA0715302 to G.H.), the National Natural Science Foundation of China (61975035 to Y.M. and 62375054 to Y.M.), and the Science and Technology Commission of Shanghai Municipality (21142200200 to Y.M. and 22ZR1405000 to G.H.).

Author affiliations: [a]Department of Materials Science & State Key Laboratory of Molecular Engineering of Polymers, Fudan University, Shanghai 200438, People's Republic of China; [b]Yiwu Research Institute of Fudan University, Yiwu, Zhejiang 322000, People's Republic of China; [c]International Institute of Intelligent Nanorobots and Nanosystems, Fudan University, Shanghai 200438, People's Republic of China; [d]State Key Laboratory of Surface Physics & Institute for Nanoelectronic Devices and Quantum Computing, Department of Physics, Fudan University, Shanghai 200438, People's Republic of China; [e]Shanghai Frontiers Science Research Base of Intelligent Optoelectronics and Perception, Institute of Optoelectronics, Fudan University, Shanghai 200438, People's Republic of China; [f]State Key Laboratory of Application-specific Integrated Circuit and System, School of Microelectronics, Zhangjiang Fudan International Innovation Center, Fudan University, Shanghai 200438, People's Republic of China; and [g]Shanghai Institute of Microsystem and Information Technology, Chinese Academy of Sciences, Shanghai 200050, People's Republic of China

1. N. Savage, Spectrometers. *Nat. Photonics* **3**, 601–602 (2009).
2. T. Oka, Spectroscopy and astronomy: H 3+ from the laboratory to the Galactic center. *Faraday Discuss.* **150**, 9–22 (2011).
3. Y. Leng, Materials Characterization: Introduction to Microscopic and Spectroscopic Methods (John Wiley & Sons, 2013).
4. S. Yuan *et al.*, Geometric deep optical sensing. *Science* **379**, eade1220 (2023).
5. Q. Cen *et al.*, Microtaper leaky-mode spectrometer with picometer resolution. *eLight.* **3**, 9 (2023).
6. J. Oliver, W.-B. Lee, H.-N. Lee, Filters with random transmittance for improving resolution in filter-array-based spectrometers. *Opt. Express* **21**, 3969–3989 (2013).
7. C. P. Bacon, Y. Mattley, R. Defrece, Miniature spectroscopic instrumentation: Applications to biology and chemistry. *Rev. Sci. Instrum.* **75**, 1–16 (2004).
8. E. Ukwatta, J. Samarabandu, M. Hall, Machine vision system for automated spectroscopy. *Mach. Vision Appl.* **23**, 111–121 (2012).
9. J. M. Hart *et al.*, "Machine vision using multi-spectral imaging for undercarriage inspection of railroad equipment" in *Proceedings of the 8th world congress on railway research*, S. V. Sawadisavi, Ed. (WCRR Organizing Committee, Seoul, Korea, 2008), pp. I.2.1.2: 1–8.
10. B. H. Kim *et al.*, Three-dimensional electronic microfliers inspired by wind-dispersed seeds. *Nature* **597**, 503–510 (2021).
11. H.-J. Yoon *et al.*, Biodegradable, three-dimensional colorimetric fliers for environmental monitoring. *Sci. Adv.* **8**, eade3201 (2022).
12. W. Bai *et al.*, Bioresorbable photonic devices for the spectroscopic characterization of physiological status and neural activity. *Nat. Biomed. Eng.* **3**, 644–654 (2019).
13. Z. Yang, T. Albrow-Owen, W. Cai, T. Hasan, Miniaturization of optical spectrometers. *Science* **371** (2021).
14. Z. Yang *et al.*, Single-nanowire spectrometers. *Science* **365**, 1017–1020 (2019).
15. S. Yuan, D. Naveh, K. Watanabe, T. Taniguchi, F. Xia, A wavelength-scale black phosphorus spectrometer. *Nat. Photonics* **15**, 601–607 (2021).
16. H. H. Yoon *et al.*, Miniaturized spectrometers with a tunable van der Waals junction. *Science* **378**, 296–299 (2022).
17. W. Deng *et al.*, Electrically tunable two-dimensional heterojunctions for miniaturized near-infrared spectrometers. *Nat. Commun.* **13**, 4627 (2022).
18. Z. Wang *et al.*, Single-shot on-chip spectral sensors based on photonic crystal slabs. *Nat. Commun.* **10**, 1020 (2019).
19. J. H. Correia, G. De Graaf, M. Bartek, R. F. Wolffenbuttel, A single-chip CMOS optical microspectrometer with light-to-frequency converter and bus interface. *IEEE J. Solid-State Circ.* **37**, 1344–1347 (2002).
20. E. J. Candes, T. Tao, Near-optimal signal recovery from random projections: Universal encoding strategies? *IEEE Trans. Inform. Theory* **52**, 5406–5425 (2006).
21. E. J. Candes, J. Romberg, T. Tao, Robust uncertainty principles: Exact signal reconstruction from highly incomplete frequency information. *IEEE Trans. Inform. Theory* **52**, 489–509 (2006).
22. D. M. Kita *et al.*, High-performance and scalable on-chip digital Fourier transform spectroscopy. *Nat. Commun.* **9**, 4405 (2018).
23. H. Li *et al.*, A near-infrared miniature quantum dot spectrometer. *Adv. Opt. Mater.* **9**, 2100376 (2021).
24. T. Sarwar, C. Yaras, X. Li, Q. Qu, P. C. Ku, Miniaturizing a chip-scale spectrometer using local strain engineering and total-variation regularized reconstruction. *Nano Lett.* **22**, 8174–8180 (2022), 10.1021/acs.nanolett.2c02654.
25. P. Wang, R. Menon, Computational spectroscopy via singular-value decomposition and regularization. *Opt. Express* **22**, 21541–21550 (2014).
26. U. Kurokawa, B. I. Choi, C.-C. Chang, Filter-based miniature spectrometers: Spectrum reconstruction using adaptive regularization. *IEEE Sens. J.* **11**, 1556–1563 (2011).
27. L. Huang, R. Luo, X. Liu, X. Hao, Spectral imaging with deep learning. *Light Sci. Appl.* **11**, 61 (2022).
28. A. Li *et al.*, Advances in cost-effective integrated spectrometers. *Light Sci. Appl.* **11**, 174 (2022).
29. X. Huang, C. Liu, P. Zhou, 2D semiconductors for specific electronic applications: From device to system. *NPJ 2D Mater. Appl.* **6**, 51 (2022).
30. M. N. Zhang *et al.*, Spectrum projection with a bandgap-gradient perovskite cell for colour perception. *Light Sci. Appl.* **9**, 162 (2020).
31. Y. Li *et al.*, A platform for integrated spectrometers based on solution-processable semiconductors. *Light Sci. Appl.* **12**, 184 (2023).
32. M. Yako *et al.*, Video-rate hyperspectral camera based on a CMOS-compatible random array of Fabry–Pérot filters. *Nat. Photonics*, **17**, 218–223 (2023), 10.1038/s41566-022-01141-5.
33. J. H. Correia, G. De Graaf, S. H. Kong, M. Bartek, R. F. Wolffenbuttel, Single-chip CMOS optical microspectrometer. *Sensors Actuators A: Phys.* **82**, 191–197 (2000).
34. E. J. Candes, M. B. Wakin, An introduction to compressive sampling. *IEEE Signal Process. Mag.* **25**, 21–30 (2008).
35. M. Ilyas, I. Mahgoub, Smart Dust: Sensor Network Applications, Architecture and Design (CRC Press, 2018).
36. J. Liu *et al.*, A near-infrared colloidal quantum dot imager with monolithically integrated readout circuitry. *Nat. Electron.* **5**, 443–451 (2022), 10.1038/s41928-022-00779-x.
37. S. Yun *et al.*, "Highly efficient color separation and focusing in the sub-micron CMOS image sensor" in *2021 IEEE International Electron Devices Meeting (IEDM)*, M.-F. Chang, S. Chowdhury, Eds. (IEEE, San Francisco, CA, 2021), pp. 30.31.31–30.31.34.
38. J. Shin *et al.*, Bioresorbable optical sensor systems for monitoring of intracranial pressure and temperature. *Sci. Adv.* **5**, eaaw1899 (2019).
39. G. Li *et al.*, Silicon nanomembrane phototransistor flipped with multifunctional sensors toward smart digital dust. *Sci. Adv.* **6**, eaaz6511 (2020).
40. C.-Y. You *et al.*, Foldable-circuit-enabled miniaturized multifunctional sensor for smart digital dust. *Chip* **1**, 100034 (2022).
41. D. Kwak, D. K. Polyushkin, T. Mueller, In-sensor computing using a MoS(2) photodetector with programmable spectral responsivity. *Nat. Commun.* **14**, 4264 (2023).
42. Z. Xuan *et al.*, On-chip short-wave infrared multispectral detector based on integrated Fabry-Perot microcavities array. *Chinese Opt. Lett.* **20**, 061302 (2022).
43. B. Wang, G. P. Wang, Plasmon Bragg reflectors and nanocavities on flat metallic surfaces. *Appl. Phys. Lett.* **87**, 013107 (2005).
44. L. Kong *et al.*, Single-detector spectrometer using a superconducting nanowire. *Nano Lett.* **21**, 9625–9632 (2021).
45. Y. August, A. Stern, Compressive sensing spectrometry based on liquid crystal devices. *Opt. Lett.* **38**, 4996–4999 (2013).
46. M. P. Edgar, G. M. Gibson, M. J. Padgett, Principles and prospects for single-pixel imaging. *Nat. Photonics* **13**, 13–20 (2019).
47. G. M. Gibson, S. D. Johnson, M. J. Padgett, Single-pixel imaging 12 years on: A review. *Opt. Express* **28**, 28190–28208 (2020).
48. T.-H. Hsu *et al.*, A 0.5-V real-time computational CMOS image sensor with programmable kernel for feature extraction. *IEEE J. Solid-State Circ.* **56**, 1588–1596 (2020).